INTERNATIONAL JOURNAL FOR NUMERICAL METHODS IN FLUIDS
Int. J. Numer. Meth. Fluids 2009; **59**:577–592
Published online 5 June 2008 in Wiley InterScience (www.interscience.wiley.com). DOI: 10.1002/fld.1835

Computation of a drastic flow pattern change in an annular swirling jet caused by a small decrease in inlet swirl

M. Vanierschot*,† and E. Van den Bulck

Mechanical Engineering Department, K. U. Leuven, Heverlee, Belgium

SUMMARY

This paper investigates the flow pattern change in an annular jet caused by a sudden change in the level of inlet swirl. The jet geometry consists of an annular channel followed by a specially designed stepped-conical nozzle, which allows the existence of four different flow patterns as a function of the inlet swirl number. This paper reports on the transition between two of them, called the 'open jet flow high swirl' and the 'Coanda jet flow.' It is shown that a small sudden decrease of 4% in inlet swirl results in a drastic and irreversible change in flow pattern. The objective of this paper is to reveal the underlying physical mechanisms in this transition by means of numerical simulations. The flow is simulated using the unsteady Reynolds-averaged Navier–Stokes (URANS) approach for incompressible flow with a Reynolds stress turbulence model. The analysis of the numerical results is based on a study of different forces on a control volume, which consists of the jet boundaries. The analysis of these forces shows that the flow pattern change consists of three different regimes: an immediate response regime, a quasi-static regime and a Coanda regime. The simulation reveals that the pressure–tangential velocity coupling during the quasi-static regime and the Coanda effect at the nozzle outlet during the Coanda regime are the driving forces behind the flow pattern change. These physical mechanisms are validated with time-resolved stereo-PIV measurements, which confirm the numerical simulations. Copyright © 2008 John Wiley & Sons, Ltd.

Received 16 October 2007; Accepted 1 April 2008

KEY WORDS: annular swirling flow; URANS; flow pattern change

1. INTRODUCTION

Swirling flows are well established in many engineering processes. The characteristics of a swirling flow field, such as regions of intense mixing, large recirculation zones and centrifugal forces, are favorable in applications such as combustion, chemical processes and cyclone separators [1, 2].

*Correspondence to: M. Vanierschot, Department of Mechanical Engineering, Division TME, Celestijnenlaan 300 A, B-3001 Heverlee, Belgium.
†E-mail: Maarten.Vanierschot@mech.kuleuven.be

Contract/grant sponsor: Onderzoeksfonds K. U. Leuven/Research Fund K. U. Leuven

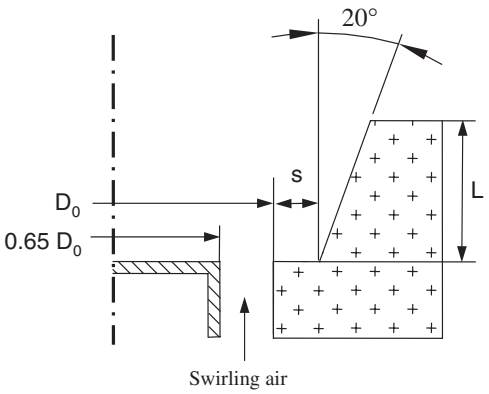

Figure 1. Schematic view of the stepped-conical nozzle.

Understanding the physical mechanisms of swirling flows is therefore crucial in controlling these different applications. Previous studies of the authors have focussed on the ability to control swirling flows. They showed that it was possible to generate four different cold flow patterns within the same jet geometry by changing the level of inlet swirl [3]. The jet geometry consists of an annular channel followed by a stepped-conical nozzle. Of great importance in this flow pattern change is the specific geometry of the in-house designed nozzle [4], which is shown in Figure 1. Swirling air enters the nozzle through an annular channel with outer diameter D_o. The nozzle consists of a sudden expansion step with height s, followed by a divergent with an opening angle of 20^o and length L. After the nozzle the jet enters the environment (free jet). The four observed flow patterns are functions of the inlet swirl and are labelled as 'closed jet flow' (CJF), 'open jet flow low swirl' (OJF-LS), 'open jet flow high swirl' (OJF-HS) and 'Coanda jet flow' (CoJF). These four flow patterns are subject to hysteresis in a swirl cycle (an increase till maximum swirl, starting from zero swirl, followed by a decrease till zero swirl). The level of swirl is represented by the swirl number S as first proposed by Beér and Chigier [2], which is defined as the ratio of the axial flux of tangential momentum to axial flux of axial momentum and outer radius,

$$S = \frac{\int_{R_i}^{R_o} 2\pi\rho U W r^2 \, dr}{R_o \int_{R_i}^{R_o} 2\pi\rho U^2 r \, dr} \tag{1}$$

where U and W are the axial and tangential velocities and R_i and R_o are the inner and outer radii of the annular channel. The hysteresis in a swirl cycle was observed experimentally; also a numerical study by Vanierschot and Van den Bulck [5] could predict the four different flow patterns and their hysteretic behavior. Figure 2 shows a comparison between their numerical simulations and experimental data in a swirl cycle. For the simulations, the Reynolds-averaged Navier–Stokes (RANS) approach is used with two turbulence models: a k–ε model and a Reynolds stress (RSTM) model. In addition, the influence of the boundary conditions is tested (uniform axial velocity or the experimentally measured velocity profile at the inlet (profile)). Starting at $S=0$, the first flow pattern is the CJF. This flow pattern evolves to an OJF-LS at intermediate swirl levels. For higher swirl number, the OJF-LS attaches to the nozzle and an OJF-HS is formed, which remains till maximum swirl ($S=0.9$, in the present case). The transition from an OJF-LS to an OJF-HS is irreversible (both experimental and numerical), since the OJF-HS will not revert back to an OJF-LS

DOI: 10.1002/fld

if the swirl is decreased to the value before the attachment. In the decrease in swirl, starting from maximum swirl, the OJF-HS changes to a CoJF, which remains till zero swirl. Again this transition is irreversible in both the experimental and numerical calculations: the CoJF will not revert back to an OJF-HS if the swirl is increased to the value before the transition. Both turbulence models predict the hysteresis and the four different flow patterns equally well.

The present computational study in this paper focusses on the transient flow pattern change from the OJF-HS (flow pattern A in Figure 2) to the CoJF (flow pattern B) in the decrease of swirl. The streamlines of both steady-state flow patterns are shown in Figure 3. The objective is

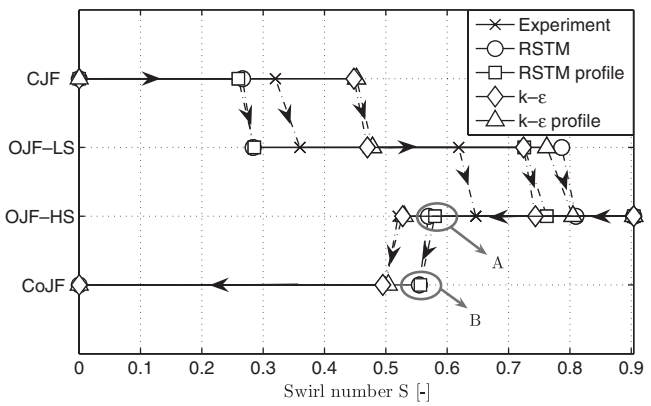

Figure 2. Transition map of a swirl cycle (an increase till maximum swirl starting from zero swirl, followed by a decrease till zero swirl). A indicates the flow pattern at the start and B indicates the flow pattern at the end of the simulation in this study. The picture is taken from [5].

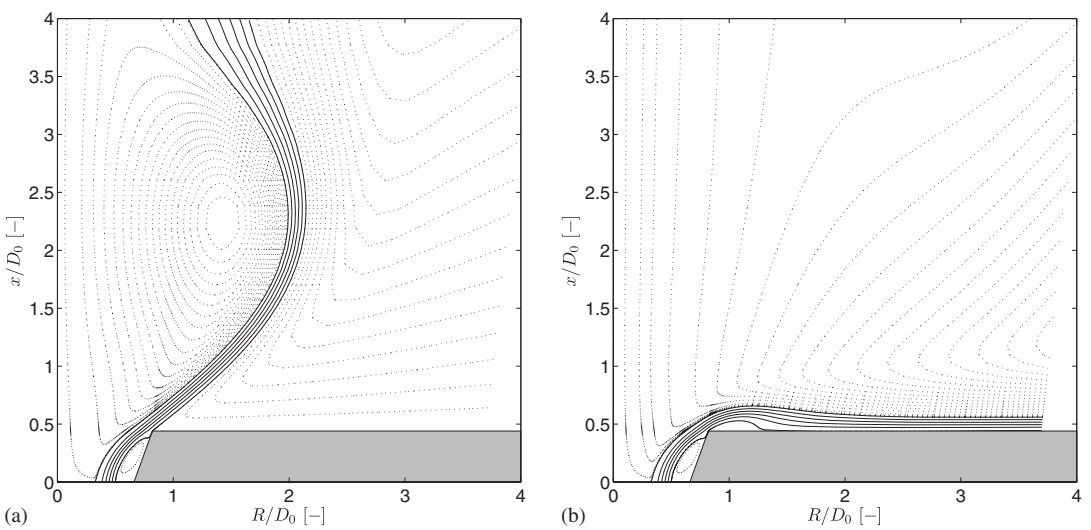

Figure 3. Streamlines for the OJF-HS and CoJF (obtained by simulation). The solid lines represent jet streamlines and the dashed lines represent recirculating and entrainment streamlines: flow patterns (a) A (OJF-HS at $S=0.58$) and (b) B (CoJF at $S=0.557$) in Figure 2.

DOI: 10.1002/fld

to reveal the underlying physics that is responsible for this drastic and remarkable change in flow pattern. The initial condition of the transient simulation is the steady-state solution of the OJF-HS (flow pattern A). Then, the inlet velocity profiles are suddenly changed from $S=0.58$ to 0.557, for which the CoJF occurs (flow pattern B). Therefore, the numerical study simulates the transient response of the OJF-HS to a sudden decrease in the inlet swirl level. The computations end when the steady-state CoJF is reached. In order to understand the physical mechanism responsible for this important flow pattern transition, an alternative analysis is performed, where the equations of motion are integrated along a control volume using the obtained numerical data. The control volume is chosen in such a way that it consists of the jet boundaries. In this manner, it is possible to study the dynamic behavior of the different forces that act on the jet. Time-resolved stereo-PIV measurements are used to validate the simulations and to confirm the physical mechanisms behind the transition.

2. NUMERICAL PROCEDURE

2.1. Governing equations

The governing equations that describe the swirling flow are the unsteady Reynolds-averaged Navier–Stokes (URANS) equations in cylindrical coordinates. The geometry and the boundary conditions are axisymmetric, giving $\partial/\partial\theta=0$. Furthermore, the OJF-HS and CoJF have been measured with a high temporal resolution. The analysis has shown that these flow fields are stationary when the high-frequency turbulent fluctuations are time averaged [3]. No precession or similar type of flow instabilities is present because the flow is stably attached to the nozzle, as indicated in Figure 3(a). Since, during the transition, the flow field remains attached to the nozzle at all times, it is a valid assumption that the turbulence-averaged flow remains axisymmetric during the course of the transition. Therefore, the equations governing this type of flow for continuity and momentum may be expressed as

$$\frac{\partial U}{\partial x}+\frac{1}{r}\frac{\partial rV}{\partial r}=0 \tag{2}$$

$$\rho\left[\frac{\partial\phi}{\partial t}+\frac{\partial U\phi}{\partial x}+\frac{1}{r}\frac{\partial rV\phi}{\partial r}\right]=\frac{\partial}{\partial x}\left(\mu\frac{\partial\phi}{\partial x}\right)+\frac{1}{r}\frac{\partial}{\partial r}\left(r\mu\frac{\partial\phi}{\partial r}\right)+S_\phi \tag{3}$$

where U, V and W are the mean axial, radial and tangential velocities and ϕ stands for any of the momentum components U, V and rW. The source term for the momentum equation S_ϕ is defined as

$$S_U=-\frac{\partial P}{\partial x}-\frac{\partial\rho\overline{u^2}}{\partial x}-\frac{1}{r}\frac{\partial r\rho\overline{uv}}{\partial r} \tag{4}$$

$$S_V=-\frac{\partial P}{\partial r}+\frac{\rho W^2}{r}-\frac{\mu V}{r^2}-\frac{1}{r}\frac{\partial r\rho\overline{v^2}}{\partial r}+\frac{\rho\overline{w^2}}{r}-\frac{\partial\rho\overline{uv}}{\partial x} \tag{5}$$

$$S_{rW}=-\frac{2\mu}{r}\frac{\partial rW}{\partial r}-r\frac{\partial\rho\overline{uw}}{\partial x}-r\frac{\partial\rho\overline{vw}}{\partial r}-2\rho\overline{vw} \tag{6}$$

DOI: 10.1002/fld

2.2. Turbulence closure

The only unknown values in Equations (4)–(6) are the Reynolds stresses $\overline{u^2}, \overline{v^2}, \overline{w^2}, \overline{uv}, \overline{uw}$ and $\overline{vw}$. In order to solve Equation (3) they need to be known. In this study, closure is obtained by solving transport equations for the Reynolds stresses [6, 7]. The equation for $\overline{u_i u_j}$ in cartesian coordinates is given as

$$\frac{\partial \rho \overline{u_i u_j}}{\partial t} + \frac{\partial}{\partial x_k}(\rho U_k \overline{u_i u_j}) - \frac{\partial}{\partial x_k}\left(\mu \frac{\partial \overline{u_i u_j}}{\partial x_k}\right) = P_{ij} - \frac{2}{3}\rho \delta_{ij} \varepsilon + D_{\mathrm{T},ij} + \phi_{ij} \tag{7}$$

The first term $P_{ij} = -\rho(\overline{u_i u_k}(\partial U_j/\partial x_k) + \overline{u_j u_k}(\partial U_i/\partial x_k))$ is the production of the stress $\overline{u_i u_j}$ and the second term, the dissipation rate ε, is calculated by solving a transport equation. The last two terms, $D_{\mathrm{T},ij}$, the turbulent diffusion, and ϕ_{ij}, the pressure strain, need to be modelled. The model for $D_{\mathrm{T},ij}$ is a simplified version of the gradient-diffusion model as proposed by Lien and Leschziner [8]. The model used for ϕ_{ij} is the one proposed by Gibson and Launder [7].

2.3. Computational domain and boundary conditions

Figure 4 shows a schematic view of the geometry and the computational domain. Air enters the computational domain through the inlet into an annular channel with an outer diameter $D_\mathrm{o} = 87\,\mathrm{mm}$ and an inner diameter $D_\mathrm{i} = 0.65 D_\mathrm{o}$. The length of the channel $L_\mathrm{c} = 3.5 D_\mathrm{o}$. At the end, an in-house designed nozzle is placed, whose dimensions are very important for the existence of multiple flow patterns. The nozzle consists of a stepwise expansion with a height of $0.15 D_\mathrm{o}$, followed by a divergent with an axial length $L_\mathrm{D} = 0.44 D_\mathrm{o}$ and an opening angle of 20°. The nozzle is followed by a sudden expansion into a large confinement of diameter $30 D_\mathrm{o}$. The confinement is chosen large enough to simulate a free jet, and simulations with different confinement geometries show that the wall of the confinement has no influence on the velocity, pressure and turbulence profiles near the nozzle [5]. The outlet is chosen to be at $32.5 D_\mathrm{o}$. To prevent inflow through the outlet, it is partially blocked by a wall of diameter $25 D_\mathrm{o}$ at $x = 22.5 D_\mathrm{o}$, followed by a channel of length $10 D_\mathrm{o}$. This is mainly done for increasing the computational speed. Various simulations on the blocking ratio also show that it has no influence on the jet in the region of interest. The geometry

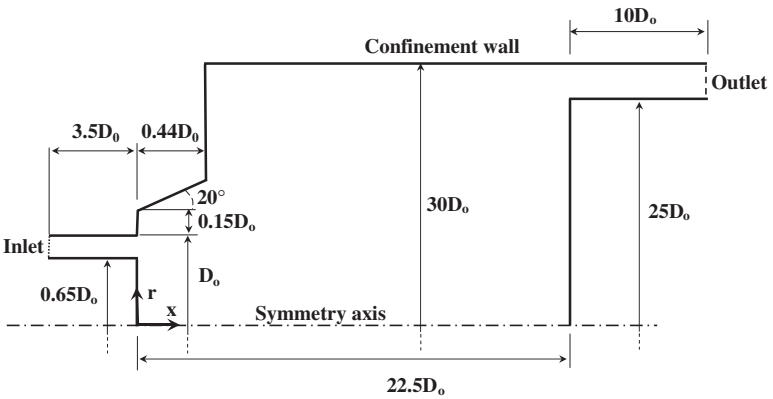

Figure 4. Schematic view of the geometry and computational domain. The thick solid lines represent wall boundaries.

DOI: 10.1002/fld

is oriented in such a way that the x-axis of a cylindrical coordinate system (x, r, θ) is coincident with the central axis of the geometry and the origin is located at the exit of the annular channel; hence, the stepwise expansion is situated at $x=0$. For the calculations, air is chosen as the working fluid with a density $\rho=1.1708\,\mathrm{kg/m^3}$ and a kinematic viscosity $v=1.85\times10^{-5}\,\mathrm{m^2/s}$. The fluid is chosen to be incompressible and Newtonian.

Previous simulations by the authors have shown that the influence of the inlet velocity profile on the prediction of the transitional swirl number from an OJF-HS to a CoJF is very small [5]. Therefore, the axial velocity profile at the inlet is chosen to be constant at $U_0=6.48\,\mathrm{m/s}$. The Reynolds number based on U_0 and the hydraulic diameter of the annular channel, $D_\mathrm{o}-D_\mathrm{i}$, is 10 650. The tangential velocity profile at the inlet is a solid body rotation, $W=\Omega r$, and the value of Ω is chosen in such a way that the inlet swirl number $S=0.557$. The Reynolds stresses at the inlet are computed based on k using the assumption of isotropy of turbulence, $\overline{u^2}=\overline{v^2}=\overline{w^2}=\frac{2}{3}k$ and $\overline{uv}=\overline{uw}=\overline{vw}=0$. The value of k is determined based on a turbulence intensity of 10%, experimentally measured [3]. At the outlet, Neumann boundary conditions for the variables are applied together with the radial pressure equilibrium, expressed as $\partial p/\partial r=\rho W^2/r$. A symmetric boundary condition is applied at the central axis. At the walls, a no-slip boundary condition is applied. The mesh near the wall is fine enough to resolve the velocity profile. The first grid point in the normal direction to the wall is well inside the viscous sub-layer resulting in a maximum y^+ of 3. The values of the Reynolds stresses at the wall are computed based on the skin friction velocity $u_\tau=\sqrt{\tau_w/\rho}$, where τ_w is the wall shear stress.

2.4. Discretization schemes

Equations (2) and (3) together with the turbulence equations are solved using the finite-volume-based solver Fluent 6.2 [9]. The spatial derivatives of the momentum and turbulence equations are discretized using the third-order MUSCL differential scheme, which improves the spatial accuracy by reducing numerical diffusion compared with second-order upwind schemes [10]. The grid consists of 60 600 cells. A detailed view of the grid inside the stepped-conical nozzle is shown in Figure 5. A grid study with a finer grid of 242 400 cells showed that the maximum relative difference in variables between the coarse and the fine grids is within 0.5% [5].

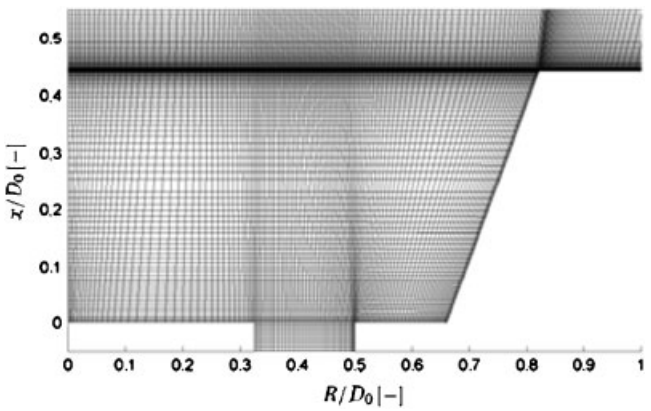

Figure 5. Detailed view of the grid inside the stepped-conical nozzle as schematically shown in Figure 1.

DOI: 10.1002/fld

The SIMPLEC algorithm is used for pressure–velocity coupling [11] and the pressure interpolation scheme is the PRESTO!-scheme [12]. The time derivative is discretized by a second-order implicit time-discretization scheme in such a way that the variable at timestep $n+1$, ϕ^{n+1}, is given by

$$\phi^{n+1} = \tfrac{4}{3}\phi^{n} - \tfrac{1}{3}\phi^{n-1} + \tfrac{2}{3}\Delta t F(\phi^{n+1}) \tag{8}$$

with $F(\phi)$ being the spatial discretization of ϕ in Equation (3). This scheme is unconditionally stable with respect to the value of the timestep Δt. However, to obtain a high temporal resolution, the value of Δt is chosen to obtain a mean cell Courant number of 3. In this manner, the flow pattern change is divided into approximately 10 000 timesteps, which is a sufficiently high temporal resolution. The convergence criterion is based on the sum of the absolute values of the mass flow residual in each cell. The solution in each timestep has converged when this sum is smaller than 5×10^{-10} kg/s.

2.5. Solution strategy

The objective of this paper is to study the underlying physics of the drastic and irreversible change in flow pattern from an OJF-HS to a CoJF caused by a small decrease in the inlet swirl. The initial condition of the transient simulation is the steady-state solution of the OJF-HS (flow pattern A in Figure 2) at $S=0.58$ in the decrease in swirl. The inlet velocity profiles of the CoJF at $S=0.557$ (flow pattern B) are applied. In this manner, the velocity field is not in equilibrium with the initial conditions and the solution strategy simulates the transient response of the steady-state OJF-HS to a sudden decrease in the inlet swirl from $S=0.58$ to 0.557. As shown later, the underlying physics in the flow pattern change is independent of the quickness of change in swirl and any kind of decrease in swirl from $S=0.58$ to 0.557 could be used. However, for simplicity a step change is chosen. The simulations end when the steady-state CoJF is reached.

3. RESULTS AND DISCUSSION

For an incompressible axisymmetric flow, the normalized streamfunction Ψ can be calculated from the axial velocity profile as

$$\Psi(x,r) = \left(\int_0^r Ur\,\mathrm{d}r\right) \Big/ \left(\int_0^{D/2} Ur\,\mathrm{d}r\right) \tag{9}$$

The projection of the velocity vector in a meridional (xr) plane is directed along the 'stream-surfaces' $\Psi(x,r)=$const., and the fluid particle paths are lines, spirals in the case of swirling flows, on these surfaces. Owing to the normalization, the 'stream-surfaces' $|\Psi|=0$ and 1 are jet boundaries and the 'stream-surfaces' $|\Psi|<0$ and $|\Psi|>1$ are recirculation zones. More details on the description of the streamfunction in axisymmetric swirling flows can be found in [13]. Let us now define two axisymmetric control volumes inside the flow as shown in Figure 6. The first one, called CV_1, is the part of the jet inside the nozzle. The outlet of the annular channel is the inlet boundary of CV_1, the boundaries on the side are Ψ_0 and Ψ_1 and the outlet boundary is the part between Ψ_0 and Ψ_1 at the nozzle outlet. The second control volume, called CV_2, is a part of the jet outside the nozzle. The inlet of CV_2 is the outlet of CV_1 and the side boundaries are Ψ_0 and Ψ_1. The outlet of CV_2 is perpendicular to Ψ_0 and Ψ_1 and is situated at a length $2D_o$ downstream of its inlet.

DOI: 10.1002/fld

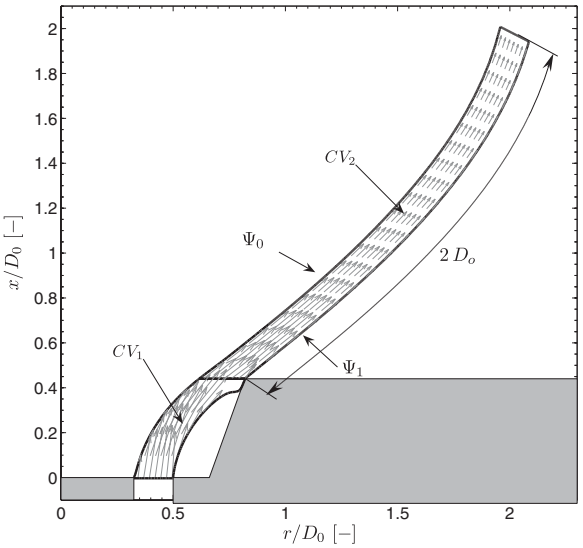

Figure 6. Steady-state OJF-HS: view of the two control volumes CV_1 (inside the nozzle) and CV_2 (outside the nozzle). The arrows represent the projected velocity vectors on a (xr)-plane inside both control volumes.

Equation (3) expresses the equilibrium of forces in a fixed point inside the flow. However, Equation (3) can also be integrated across a control volume CV, which can be CV_1 or CV_2. The expression thus obtained is called the integral form of the equations of motion. Note that the boundaries Ψ_0 and Ψ_1 are not necessarily fixed in space and that the control volumes can move and deform along with a change in flow. The velocities of a boundary are U_b in the axial direction and V_b in the radial direction. Note that for a solid boundary $U_b = V_b = 0$. The volume of CV is given by $V = 2\pi \int_0^{L_x} \int_{\Psi_0}^{\Psi_1} r\,\mathrm{d}r\,\mathrm{d}x$, where L_x is the axial length of CV. Applying the Reynolds transport theorem to CV and taking into account the movement and deforming, the momentum equations without the viscous terms are given by

$$\frac{\mathrm{d}}{\mathrm{d}t}\left[\int_0^{L_x}\int_{\Psi_0}^{\Psi_1} \rho U r\,\mathrm{d}r\,\mathrm{d}x\right] + \int_{\Gamma_x} \rho U (U-U_b) r\,\mathrm{d}r + \int_{\Gamma_r} \rho U (V-V_b) r\,\mathrm{d}x = \int_0^{L_x}\int_{\Psi_0}^{\Psi_1} S_U r\,\mathrm{d}r\,\mathrm{d}x \tag{10}$$

$$\frac{\mathrm{d}}{\mathrm{d}t}\left[\int_0^{L_x}\int_{\Psi_0}^{\Psi_1} \rho V r\,\mathrm{d}r\,\mathrm{d}x\right] + \int_{\Gamma_x} \rho V (U-U_b) r\,\mathrm{d}r + \int_{\Gamma_r} \rho V (V-V_b) r\,\mathrm{d}x = \int_0^{L_x}\int_{\Psi_0}^{\Psi_1} S_V r\,\mathrm{d}r\,\mathrm{d}x \tag{11}$$

where Γ_x represent the projected surfaces of CV with a normal in the axial direction and Γ_r represent with a normal in the radial direction. Consider now a frame of reference moving along

DOI: 10.1002/fld

with CV. The left and right boundaries of CV are streamlines; hence, no momentum enters through these boundaries if CV is stationary. In the case of a moving CV, the first term of Equations (10) and (11) is equal to the momentum flux caused by the relative velocity difference $U-U_\mathrm{b}$ or $V-V_\mathrm{b}$ between boundary and fluid velocities of the moving and deforming CV. In other words, Equations (10) and (11) can be simplified to

$$\int_{\Gamma_x} \rho U^2 r\,\mathrm{d}r + \int_{\Gamma_r} \rho U V r\,\mathrm{d}x = \int_0^{L_x}\int_{\Psi_0}^{\Psi_1} S_U r\,\mathrm{d}r\,\mathrm{d}x \tag{12}$$

$$\int_{\Gamma_x} \rho V U r\,\mathrm{d}r + \int_{\Gamma_r} \rho V V r\,\mathrm{d}x = \int_0^{L_x}\int_{\Psi_0}^{\Psi_1} S_V r\,\mathrm{d}r\,\mathrm{d}x \tag{13}$$

By applying Gauss's theorem, $\iiint_V \nabla\cdot\mathbf{f}\,\mathrm{d}V = \iint_A \mathbf{f}\cdot\mathrm{d}\mathbf{A}$, where $\nabla\cdot\mathbf{f}=[\partial f_x/\partial x, 1/r\,\partial(rf_r)/\partial r]$ and $\mathrm{d}\mathbf{A}$ is the surface vector of the boundary of V, to the right-hand side of Equations (12) and (13), taking into account the following relation:

$$\frac{\partial p}{\partial r} = \frac{1}{r}\frac{\partial r p}{\partial r} - \frac{p}{r} \tag{14}$$

one can obtain an expression for the integral form of the axial momentum equation as

$$\underbrace{\int_{\Gamma_x} \rho U^2 r\,\mathrm{d}r + \int_{\Gamma_r} \rho U V r\,\mathrm{d}x}_{\dot{M}_x} = \underbrace{-\int_\Gamma p r\,\mathrm{d}r}_{F_{p,x}} \underbrace{-\int_\Gamma \rho\overline{u^2} r\,\mathrm{d}r}_{F_{\overline{uu}}} \underbrace{-\int_\Gamma \rho\overline{uv} r\,\mathrm{d}x}_{F_{\overline{uv},x}} \tag{15}$$

with all the variables evaluated at the boundaries Γ of the control volume CV and the integration done over every boundary of CV. On the left-hand side, $\dot{M}_x$ is the change in axial momentum of CV. On the right-hand side, the first term is the pressure force acting on the boundaries of CV, called F_p. The last two terms are the forces on CV due to the turbulence, $F_{\overline{uu}}$ and $F_{\overline{uv}}$. The expression for the radial momentum equation is in a similar manner given by

$$\underbrace{\int_{\Gamma_x} \rho V U r\,\mathrm{d}r + \int_{\Gamma_r} \rho V^2 r\,\mathrm{d}x}_{\dot{M}_r} = \underbrace{-\int_\Gamma p r\,\mathrm{d}x + \int_0^{L_x}\int_{\Psi_0}^{\Psi_1} p\,\mathrm{d}r\,\mathrm{d}x}_{F_{p,r}} + \underbrace{\int_0^{L_x}\int_{\Psi_0}^{\Psi_1} \rho(W^2+\overline{w^2})\,\mathrm{d}r\,\mathrm{d}x}_{F_\mathrm{c}}$$
$$\underbrace{-\int_\Gamma \rho\overline{v^2} r\,\mathrm{d}x}_{F_{\overline{vv}}} \underbrace{-\int_\Gamma \rho\overline{uv} r\,\mathrm{d}r}_{F_{\overline{uv},r}} \tag{16}$$

In this expression, the left-hand side $\dot{M}_r$ is the change in radial momentum of CV. On the right-hand side, an extra term F_c appears, which is the centrifugal body force due to the rotation of the jet. The remaining terms are equivalent to those in Equation (15).

3.1. Steady-state OJF-HS

The forces on CV_1 and CV_2 for the steady-state OJF-HS, as defined in Equations (15) and (16), are shown in Table I(a) and (b). The values are scaled with regard to the axial momentum at

DOI: 10.1002/fld

Table I. Strength of the different forces on CV_1 and CV_2 for the steady-state OJF-HS.

	x-Direction (%)	r-Direction (%)		x-Direction (%)	r-Direction (%)
(a) *Forces on* CV_1					
$\dot{M}_{in}$	−100	−12.24	F_p	−22.43	26.55
$\dot{M}_{out}$	46.89	58.37	F_c	0	30.96
			F_{Rey}	−29.45	−11.55
(b) *Forces on* CV_2					
$\dot{M}_{in}$	−46.89	−58.37	F_p	+17.24	−31.5
$\dot{M}_{out}$	23.52	5.9	F_c	0	14.66
			F_{Rey}	−39.46	−36.36

The values are scaled with the inlet momentum in the axial direction of CV_1. F_{Rey} is the turbulent force due to the Reynolds stresses.

the inlet of CV_1. The momentum deficit is about 1.2% in the axial direction and about 1.4% in the radial direction of the incoming momentum for CV_1 and, respectively, 2.5 and 1.25% for CV_2. This deficit is caused by neglecting the viscous forces and by interpolation errors, since the boundaries of the control volumes are not coincident with the cell centers. However, at each timestep in the numerical calculation, the deficit in axial and radial momentum remains below the values mentioned above.

As can be seen in Table I(a), the jet loses 53.11% of its axial momentum when it exits the nozzle. This decay is more or less in equal amounts caused by the pressure forces and the Reynolds stresses on the boundaries. The radial momentum at the outlet is more than 4.5 times larger than the radial momentum at the inlet. This increase is mostly caused by the centrifugal force F_c and the pressure force F_p on the boundaries. The Reynolds stresses are much smaller compared with those two. As the jet exits the annular channel, a 'corner recirculation zone' (CRZ) is formed between the sudden expansion and the nozzle divergent (Figure 6). The sub-pressure inside this CRZ is the largest part of F_p and, as shown later, plays an important role in the transition as it keeps the jet attached to the nozzle. Outside the nozzle (CV_2) the Reynolds stresses are substantially higher than inside the nozzle. In this region, the centrifugal force is also much smaller. However, as shown later, the Reynolds stresses do not play an important role in the physics of the transition.

The tangential velocity and pressure field of the steady-state OJF-HS outside the nozzle are shown in Figure 7 (solid black lines). The streamlines of the OJF-HS are shown as gray lines. The solid gray lines represent jet streamlines and the dashed gray lines represent recirculation and entrainment zones. In the flow field downstream of the nozzle, a pressure field is created to balance the centrifugal forces, given by the simplified radial momentum equation

$$\frac{\partial p}{\partial r} = \rho \frac{W^2}{r} \tag{17}$$

Integrating the above equation starting at $r = \infty$ results in a pressure along the central axis ($r = 0$), which is lower compared with the environmental pressure at $r = \infty$ (Figure 7(b)). This sub-pressure at the central axis bends the OJF-HS streamlines towards the center further downstream. As a consequence, a large central torroidal vortex (CTV) is created, whose center is situated at $x = 2.26 D_o$ and $r = 1.44 D_o$. For an inviscid flow, the angular momentum rW along a streamline is constant. Hence, the rotating CTV induces a region of high tangential velocity near the axis (between 2 and $3.5 D_o$) where its streamlines reach their minimum radius. Because of the coupling

DOI: 10.1002/fld

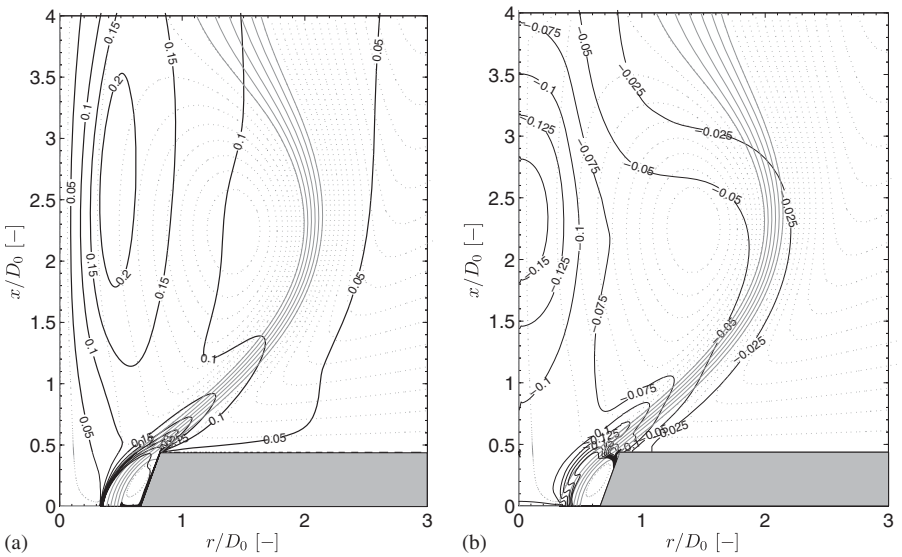

Figure 7. Tangential velocity and pressure field of the steady-state OJF-HS at $S=0.58$. The streamlines are given as gray lines in the background: (a) dimensionless tangential velocity field W/U_0 and (b) dimensionless pressure field $(P-P_\infty)/(0.5\rho U_0^2)$.

between pressure and tangential velocity (Equation (17)), this region of high tangential velocity at low radius minimizes the pressure at the central axis at $x/D_o \approx 2.3$.

3.2. Transition from an OJF-HS to a CoJF

The transition from an OJF-HS to a CoJF can be divided into three regimes. The first one is called the 'immediate response regime.' In this regime ($0 \leqslant T \leqslant 8$), the jet responds to the sudden step change in the inlet swirl. The dimensionless time $T = tU_0/L_c$ is defined in such a way that a particle at the inlet with constant velocity U_0 reaches the nozzle at $T=1$. The oscillations of the variables in the flow field damp out in time and the transition enters the second regime, called the 'quasi-static regime' ($8 < T \leqslant 167$). In this regime, the changes and time derivatives of the variables in the flow field are very slow compared with those in the response regime. The 'quasi-static' regime ends when the Coanda effect takes place at the nozzle outlet. The transition enters the last regime for $T > 167$, called the Coanda regime, and the flow field evolves towards the steady-state CoJF at $S=0.557$.

3.2.1. Immediate response regime ($0 \leqslant T \leqslant 8$). The first regime in the simulation is the immediate response regime. This regime covers the response of the jet flow to the sudden step change in the inlet swirl. Figure 8 shows the time derivative of the volume-integrated axial U (dashed line) and radial V (solid line) velocity inside CV_1 as a function of T (first term in Equations (10) and (11)). These terms correspond to the inertial forces on CV_1 in the axial and radial directions for an observer moving along with CV_1. Both values shown are scaled with the inlet axial momentum at $T=0$ (the steady-state OJF-HS). The movement of CV_1 is only in the radial direction since the

DOI: 10.1002/fld

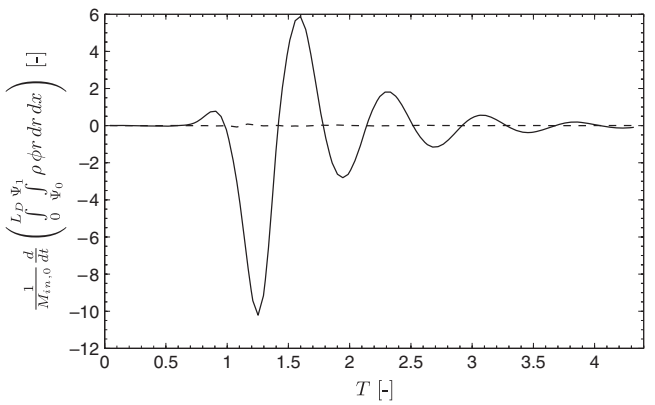

Figure 8. Time derivative of the volume-integrated value of ϕ (inertial force for an observer moving along with CV), scaled with the axial momentum of the steady-state OJF-HS at the inlet. Solid line: $\phi = V$ and dashed line: $\phi = U$.

first term in Equation (10) can be expressed as

$$\frac{\mathrm{d}}{\mathrm{d}t}\left[\int_0^{L_x}\int_{\Psi_0}^{\Psi_1}\rho U r\,\mathrm{d}r\,\mathrm{d}x\right] = \frac{\mathrm{d}(\int_0^{L_x}\dot{m}_0\,\mathrm{d}x)}{2\pi\,\mathrm{d}t} = \frac{\mathrm{d}(\dot{m}_0 L_x)}{2\pi\,\mathrm{d}t} = 0 \tag{18}$$

where $\dot{m}_0$ is the mass flow rate of the jet. The sudden change in the inlet swirl is convectively transported towards CV_1 and it is first noticeable at $T = 0.75$, corresponding to a convective velocity of $U \approx 1.33U_0$, which is higher than the maximum axial velocity inside the annular channel ($1.19U_0$). The maximum inertial force on CV_1 is approximately 10 times the axial momentum flux at the inlet and dims out exponentially in time. The immediate response regime is of no further interest as it is the response of the OJF-HS to the step change in the inlet swirl and the physical effects responsible for the change in the flow pattern take place during the quasi-static and Coanda regime. The duration of this regime ($\Delta T = 8$) is also much smaller compared with that of the quasi-static regime ($\Delta T = 159$).

3.2.2. Quasi-static regime ($8 < T \leqslant 167$). In the quasi-static regime, the inertial forces are below 1.5% of the axial momentum at the inlet; hence, this regime is called quasi-static. The changes in the flow field in the quasi-static regime take place outside the nozzle. In this region, the simple radial equilibrium equation (Equation (17)) links the tangential velocity field with the pressure field (both shown in Figure 7). What happens if the equilibrium between pressure and centrifugal force in the steady-state OJF-HS is disturbed by a decrease in inlet swirl? Integrating Equation (17) in the radial direction and differentiating in time result in

$$\frac{\partial p}{\partial t} = \int_\infty^r 2\rho\frac{W}{r}\frac{\partial W}{\partial t}\,\mathrm{d}r \tag{19}$$

The above equation states that a decrease in tangential velocity results in an increase in static pressure. If the inlet swirl is decreased, the CTV will rotate less. Since rW is constant along a

DOI: 10.1002/fld

streamline of the CTV, the highest velocity gradients in time are situated near the high-velocity region in Figure 7(a), as shown in Figure 9(a). As a consequence of Equation (19), the time derivatives of pressure are the highest in this high-velocity region (high tangential velocity and high time derivative at low radius) as can be seen by comparing Figure 9(a) with (b). This increase in static pressure at the center in turn results in a smaller deflection of the streamlines further downstream, e.g. the jet expands more radially. Since rW is constant along a streamline of the jet, this increased radial expansion results in a smaller tangential velocity of the jet. This smaller tangential velocity in turn increases the static pressure at the center and so on. This mechanism of pressure–tangential velocity coupling enlarges the size of the CTV and moves its center radially outward as can be seen in Figures 10(a)–(g). This figure shows the streamlines of the jet as a function of T during the simulation. The path of the center of the CTV is given by the gray line and its position is marked with an x. The pressure–tangential velocity coupling results in an outward movement of the center in time due to the increased radial expansion of the jet. As the Coanda effect takes place at the nozzle outlet, the vortex center is pulled down, followed by a radial outward movement due to the 'roll-down' of the jet along the nozzle outlet wall (see the following section).

Figure 11 shows the forces on CV_2 as defined in Equations (15) and (16). The variables are scaled with the axial momentum at the outlet of the annular channel at $T=0$. During the quasi-static regime, the pressure–tangential velocity coupling reduces the magnitude of the pressure forces on the boundaries of the jet by more than a third. The change in centrifugal force and Reynolds stresses is small compared with the reduction in the magnitude of F_p. Although the force of the Reynolds stresses on the boundaries is high, it does not play an important role in the transition and the main driving mechanism is the pressure–tangential velocity coupling. The analysis of the

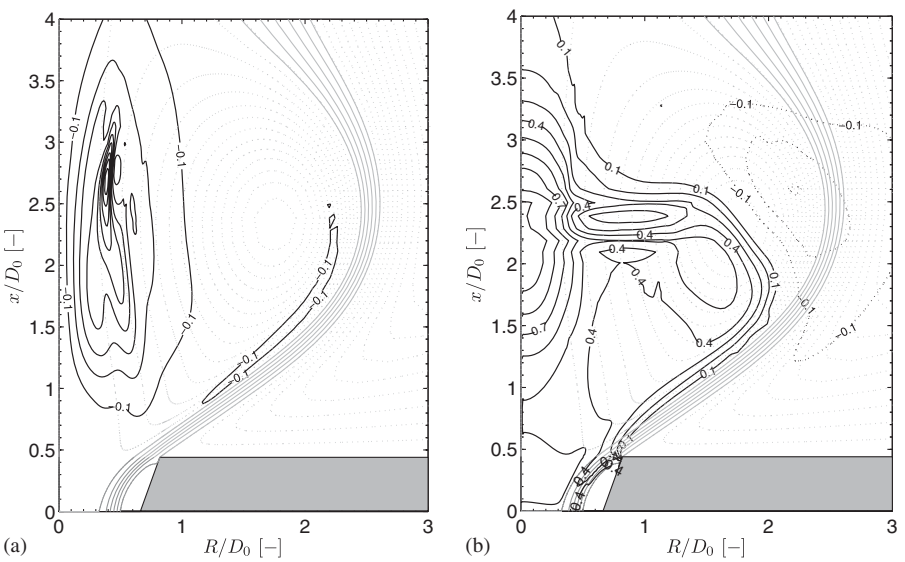

Figure 9. Dimensionless time derivative of the tangential and pressure fields at $T=43.2$. The difference between two neighboring contours is 0.1: (a) $(\partial W/\partial t)/(\partial W/\partial t)|_{\max}$ and (b) $(\partial P/\partial t)/(\partial P/\partial t)|_{\max}$.

DOI: 10.1002/fld

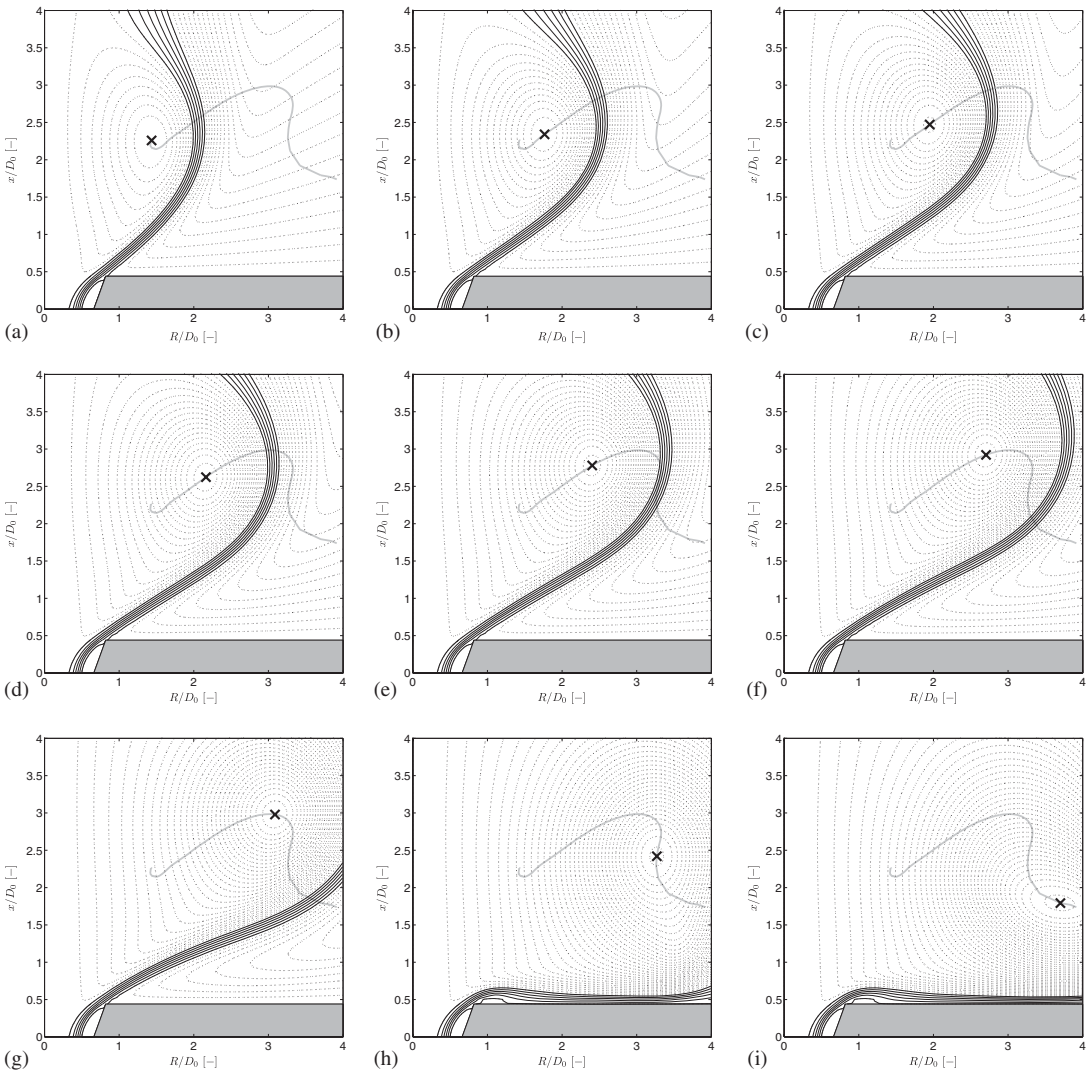

Figure 10. Streamlines of the jet flow during the transition as a function of the dimensionless time $T = tU_0/L_c$. The center of the torroidal vortex is marked with an x and its path is shown by a gray line: (a) $T = 0$; (b) $T = 43.2$; (c) $T = 64.8$; (d) $T = 86.4$; (e) $T = 108$; (f) $T = 129.6$; (g) $T = 151.2$; (h) $T = 172.8$; and (i) $T = 177.1$.

pressure forces on CV_1 shows that the pressure force of the CRZ is the highest contribution to F_p. The magnitude of this force decreases with decreasing swirl (not shown here). The role of the CRZ is important since it keeps the jet attached to the nozzle and if the dimensions of the sudden expansion are too large, the jet will detach from the nozzle before the Coanda effect can take place [4].

DOI: 10.1002/fld

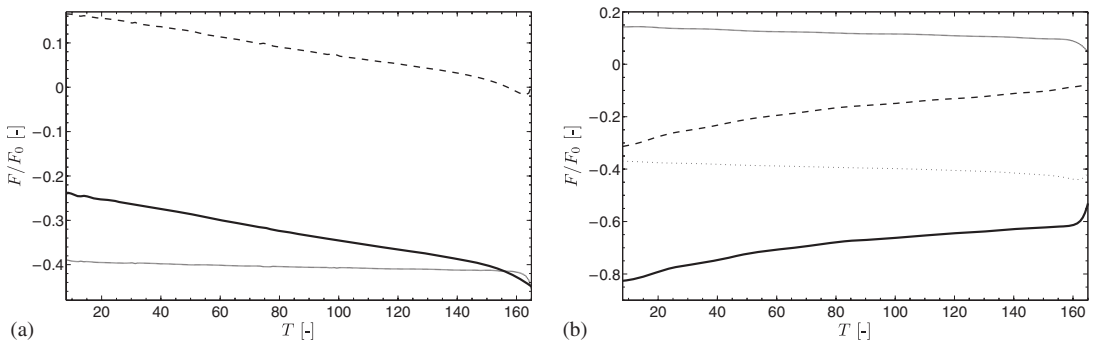

Figure 11. Terms of the axial and radial momentum equilibrium as defined in Equations (15) and (16) on CV_2. Solid line: $\dot{M}$; dashed line: F_p; dotted line: F_{Rey}; and dashed-dotted line: F_c. (a) Axial momentum equilibrium and (b) radial momentum equilibrium.

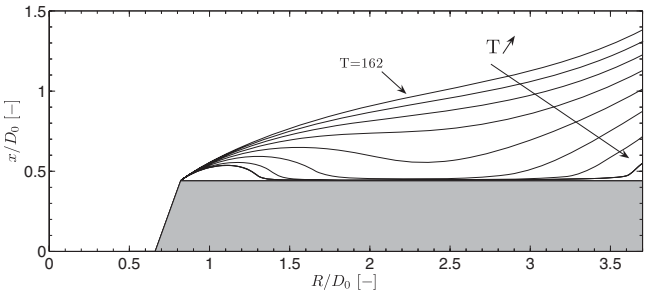

Figure 12. Boundary Ψ_1 of the jet as a function of T. The starting streamline is at $T=162$ and the time ΔT between two successive streamlines is 1.

3.2.3. Coanda regime ($T>167$). As described above, the jet will expand more radially in time due to the decreasing pressure in the region of the CTV. During the quasi-static regime, the pressure force on the outer boundary of the jet Ψ_1 remains more or less constant for $T\leqslant 140$, followed by a rapid increase. This jet boundary Ψ_1 at different times T near the transition to the Coanda regime is shown in Figure 12. The time interval ΔT between two successive streamlines is 1. The figure shows the shrinking of the region of entrainment between the jet boundary Ψ_1 and the wall of the nozzle due to the increased radial expansion. This shrinking increases the velocity in the entrainment zone between CV_2 and the wall. According to the law of Bernoulli, this increased velocity decreases the static pressure in the region of entrainment (not shown in the figure). This decrease in pressure pulls the jet even more towards the wall and so on. This effect is known as the Coanda effect and at $T=167$ the jet attaches to the wall. This attachment is the start of the Coanda regime. In this regime the jet rolls down the wall in the outward radial direction and evolves towards the steady-state CoJF. This Coanda effect is validated based on time-resolved stereo-PIV measurements and the streamlines of the measured velocity profiles confirm the above-explained physical mechanisms of the Coanda effect and the 'roll-down' of the jet along the nozzle wall [14]. The simulation has thus revealed correctly the underlying physics.

DOI: 10.1002/fld

4. CONCLUDING REMARKS

In this paper a numerical simulation has been made of the flow pattern transition of an annular swirling jet caused by a sudden change in the inlet swirl from $S=0.58$ to 0.557. The flow was simulated using the URANS approach with an RSTM turbulence model. The equations of motion are integrated across a control volume CV, consisting of the jet boundaries. The simulation has shown that the transition can be divided into three regimes: the immediate response regime, the quasi-static regime and the Coanda regime. During the immediate response regime, the flow is dominated by large inertial forces, which can be as high as 10 times the axial momentum of the jet at the inlet. These inertial forces dim out in time and the jet enters the second regime, the quasi-static regime. In this regime the inertial forces are less than 1.5% of the incoming axial momentum. An analysis of the forces on CV shows that the pressure–tangential velocity coupling outside the nozzle results in an increased radial expansion of the jet. If the radial expansion is large enough, the Coanda effect takes place at the nozzle outlet and the jet is pulled towards the outlet wall of the nozzle. In this third and last regime, called the Coanda regime, the flow pattern evolves towards the steady-state CoJF. These physical mechanisms are validated by time-resolved stereo-PIV measurements and the streamlines of the measured velocity profiles confirm the numerical simulation. The simulation has thus revealed correctly the underlying physics of the transition.

ACKNOWLEDGEMENTS

The authors gratefully acknowledge the funding of this work by the Onderzoeksfonds K. U. Leuven/ Research Fund K. U. Leuven.

REFERENCES

1. Gupta AK, Lilley DG, Syred N. *Swirl Flows*. Abacus Press: Tunbridge Wells, U.K., 1984.
2. Beér J, Chigier N. *Combustion Aerodynamics*. Krieger: New York, 1983.
3. Vanierschot M, Van den Bulck E. Hysteresis in flow patterns in annular swirling jets. *Experimental Thermal and Fluid Science* 2007; **31**:513–524.
4. Vanierschot M, Van den Bulck E. Influence of the nozzle geometry on the hysteresis of annular swirling jets. *Combustion Science and Technology* 2007; **179**(8):1451–1466.
5. Vanierschot M, Van den Bulck E. Numerical study of hysteresis in annular swirling jets with a stepped-conical nozzle. *International Journal for Numerical Methods in Fluids* 2007; **54**:313–324.
6. Launder BE, Reece GJ, Rodi W. Progress in the development of a Reynolds stress turbulence closure. *Journal of Fluid Mechanics* 1975; **68**(3):537–566.
7. Gibson MM, Launder BE. Ground effects on pressure fluctuations in the atmospheric boundary layer. *Journal of Fluid Mechanics* 1978; **86**:491–511.
8. Lien FS, Leschziner MA. Assessment of turbulent transport models including non-linear RNG eddy-viscosity formulation and second-moment closure. *Computers and Fluids* 1994; **23**(8):983–1004.
9. Fluent Inc. *Fluent 6.2 User's Guide.* Fluent Inc., January 2005.
10. Van Leer B. Toward the ultimate conservative difference scheme. IV. A second order sequel to Gudunov's method. *Journal of Computational Physics* 1979; **32**:101–136.
11. Vandoormaal JP, Raithby GD. Enhancements of the SIMPLE method for predicting incompressible fluid flows. *Numerical Heat Transfer* 1984; **7**:147–163.
12. Pantakar SV. *Numerical Heat Transfer and Fluid Flow*. Hemisphere: Washington, DC, 1980.
13. Batchelor GK. *An Introduction to Fluid Dynamics*. Cambridge University Press: Cambridge, 1973; 543–547.
14. Vanierschot M. Fluid mechanics and control of annular jets with and without swirl. *Ph.D. Thesis*, Katholieke Universiteit Leuven, 2007. (Available from: http://hdl.handle.net/1979/873.)

DOI: 10.1002/fld